RSC Advances

PAPER

View Article Online
View Journal | View Issue

Cite this: *RSC Adv.*, 2020, **10**, 4080

First principles study of ferroelectric hexagonal compounds $RInO_3$ (R = Dy, Er, and Ho): electronic structure, optical and dielectric properties

Yifei Yu,[a] Na Lin,[*ab] Haoyuan Wang,[a] Ran Xu,[a] Hao Ren[c] and Xian Zhao[*a]

Received 30th September 2019
Accepted 8th January 2020

DOI: 10.1039/c9ra07920c

rsc.li/rsc-advances

The 4f-shell electrons of rare-earth ion R have a certain influence on both the electrical and optical properties of $RInO_3$. We have studied the electronic structures, optical and dielectric properties of hexagonal compounds $RInO_3$ (R = Dy, Ho, and Er) by performing first principles calculations. After optimization, the lattice parameters are in great agreement with the experiment with an error within 1%. Band structure calculations reveal decreasing band gaps with the increase of atomic number, yielding the highest conductivity for $ErInO_3$, which has the smallest band gap in the present study. We have calculated the density of states of $RInO_3$ and characterized the displacement of In and O. The dielectric properties and ionic contribution have been calculated and a detailed comparison has been made on the dielectric function including the static dielectric tensor. The absorption coefficient, the reflectivity, the refractive index, the conductivity and the electron energy-loss spectrum of hexagonal $DyInO_3$, $HoInO_3$ and $DyInO_3$ have been calculated and analyzed.

1 Introduction

A group of materials with hexagonal ABO_3-type structure have been extensively invoked for their geometric multiferroic characteristics and potential applications in capacitors, FRAM storage, computer memory and other multifunctional devices.[1–4] Research on these materials mainly pays attention to the correlation between ferromagnetism and ferroelectricity, however, rarely does a study exist on their optical and dielectric properties which are also important to explore. It is worth noting that there are some ABO_3 perovskites reflecting superior dielectric properties[5,6] which have potential applications in manufacturing dielectric devices. People can control the dielectric and optical properties of the perovskite structures by selecting appropriate A and B cations due to the fact that physical properties of ABO_3 perovskite depend on the mass and ionic radius of the A and B cations.

Among the ABO_3 perovskite structures, $RMnO_3$ (R = rare-earth element) has been widely studied due to its excellent ferroelectric and dielectric properties,[7–13] and hexagonal $RInO_3$ with the space group of $P6_3cm$ is isomorphic to the hexagonal $RMnO_3$.[14] If we replace Mn^{3+} ions with non-transition metal In^{3+} ions, the dielectric and optical properties of the $RInO_3$ perovskite system are only contributed by the 4f-shell electrons of the rare-earth ions R^{3+},[15–21] which makes it much more straightforward to study the optical and dielectric properties of $RInO_3$ than in $RMnO_3$. Studies have shown that the spontaneous polarization of hexagonal $RInO_3$ increases with the increase of the atomic number of rare-earth elements.[22] In order to explore the dielectric and optical properties as a function of the atomic number of rare-earth elements, in present study we have chosen Dy, Ho and Er with increasing atomic number. Moreover, the hexagonal $DyInO_3$ and $HoInO_3$ are stable at normal pressure and temperature but transform to 6% denser pseudohexagonal orthorhombic phases at 20 kbar, 1000 °C,[23] while the properties of $ErInO_3$ have not yet been confirmed. In this work, we have performed first principles calculations on the electronic structure, optical and dielectric properties of hexagonal $RInO_3$ (R = Dy, Ho, and Er) and further discussed their potentials in the preparation of high quality multifunctional devices.

2 Computational details

All calculations in present paper are based on density functional theory (DFT) with Perdew–Burke–Ernzerhof (PBE) of the generalized gradient approximation (GGA)[24] functional for the exchange–correlation function, implemented in Vienna *Ab initio* Simulation Package (VASP)[25,26] by solving the Kohn–Sham equation and corrected the results by the GW method of quasi-particle approximation. The specific Kohn–Sham equation is as follows,

$$\left\{-\frac{1}{2}\nabla^2+\left[V\left(\vec{r}\right)+\mu_{xc}(n)\right]\right\}\varphi_i\left(\vec{r}\right)=\varepsilon_i\varphi_i\left(\vec{r}\right) \quad (1)$$

[a]State Key Laboratory of Crystal Materials, Shandong University, 250100 Jinan, Shandong, PR China. E-mail: linnakth@gmail.com; xianzhao@sdu.edu.cn
[b]Department of Chemistry, University of Calgary, T2N 1N4 Calgary, Alberta, Canada
[c]State Key Laboratory of Heavy Oil Processing, Center for Bioengineering and Biotechnology, China University of Petroleum (East China), 266580 Qingdao, PR China

where $V(\vec{r}) + \mu_{xc}(n) = V_{eff}(r)$ is the effective potential and ε_i is the eigenvalue of the Kohn–Sham equation. We employ the projector augmented-wave (PAW) method to describe the interaction of ions and electrons. The cut-off energy in the plane-wave expansion has been set to 450 eV, which had been accurately proved to ensure the well-converged total energy.[27] In order to obtain the well-polymerized geometrical configurations, we fully relaxed the hexagonal structures with a $5 \times 5 \times 2$ k-point mesh grid and $8 \times 8 \times 3$ for the subsequent calculations of properties. Convergences of energy and force have been respectively set to 0.01 meV per cell and -0.02 eV A^{-1}. We have also employed the density functional perturbation theory (DFPT) with a linear response method implemented in the Cambridge Serial Total Energy (CASTEP)[28] code in the calculations for optical and dielectric properties. The calculated lattice parameters of $RInO_3$ (R = Dy, Ho, Er) has been determined to be $a = b = 6.357$ Å, $c = 12.404$ Å, which are in great agreement with the experimental value of $a = b = 6.300$ Å and $c = 12.300$ Å,[29] with an error within 1%, indicating the accuracy of present calculations.

3 Results and discussion

3.1 Electronic structure of hexagonal $DyInO_3$, $HoInO_3$ and $ErInO_3$

The optimized geometrical configurations for hexagonal $RInO_3$ is shown in Fig. 1(a), containing 6 rare-earth (R) atoms, 18 oxygen (O) atoms and 6 indium (In) atoms. A $2 \times 2 \times 1$ super-cell of $RInO_3$ has been made for a better understanding, as shown in Fig. 1(b). We can see that the structure of $RInO_3$ along c-axis direction is formed by the alternating bonding of In and O atoms with hexagonal structure, and the bond length of In–O is 2.11 Å. Therefore, hexagonal $RInO_3$ has been proved to be quite stable which lays the foundation for further study on its optical and dielectric properties.

The calculated band structure of hexagonal $RInO_3$ (R = Dy, Ho, Er) is shown in Fig. 2. We position the Fermi level corresponding to the top of the valence band at zero energy and marked with dotted line. From Fig. 2 we can see that hexagonal $RInO_3$ are indirect band gap crystals with band-gap values respectively to be 1.90 eV, 1.85 eV and 1.80 eV for $DyInO_3$, $HoInO_3$ and $ErInO_3$, which reveals decreasing band gaps with the increase of atomic number. The smaller the band gap, the easier it is for the electron to be excited by the valence band to the conduction band, and the higher the conductivity. Among three crystals in present study, $DyInO_3$ which has the largest band gap will give the smallest conductivity, whereas $ErInO_3$ which has the smallest band gap yields highest conductivity.

Fig. 3 shows the total density of states (TDOS) and the partial density of states (PDOS) of unit-cell hexagonal $DyInO_3$, $HoInO_3$ and $ErInO_3$. Due to the similarity between these three crystals and the properties of the lanthanides compound, it's not difficult to observe from Fig. 3(a), (c) and (e) that the curves of total density of states of $DyInO_3$, $HoInO_3$ and $ErInO_3$ are roughly similar and there only exist minor different density peak in the energy range from -27 to -20 eV. In addition to observing the overall state density distribution, we also plot the distribution of

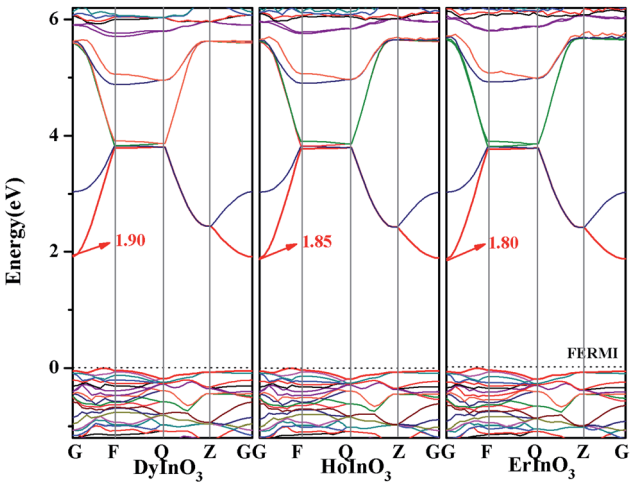

Fig. 2 Band structure of hexagonal $DyInO_3$, $HoInO_3$ and $ErInO_3$ along the high symmetry direction. The Fermi level is positioned at zero energy and marked with dotted line.

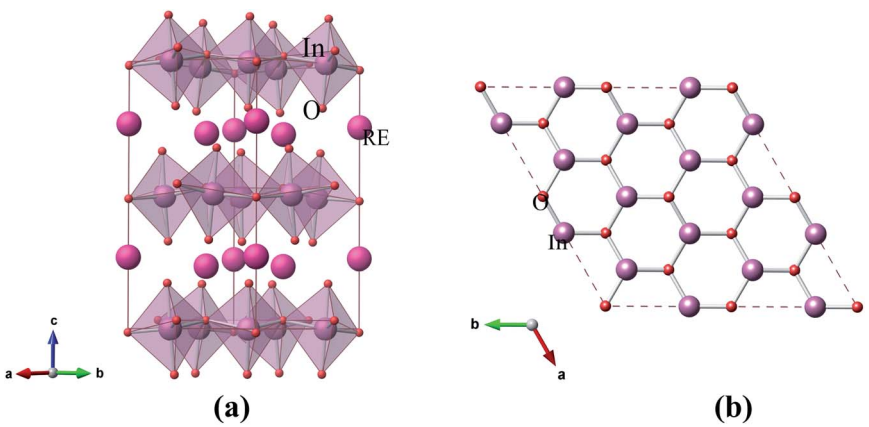

Fig. 1 (a) Optimized structure of hexagonal $RInO_3$ (R = Dy, Er, Ho). (b) Quadrilateral arrangement of a $2 \times 2 \times 1$ super-cell of optimized hexagonal $RInO_3$ along c-axis.

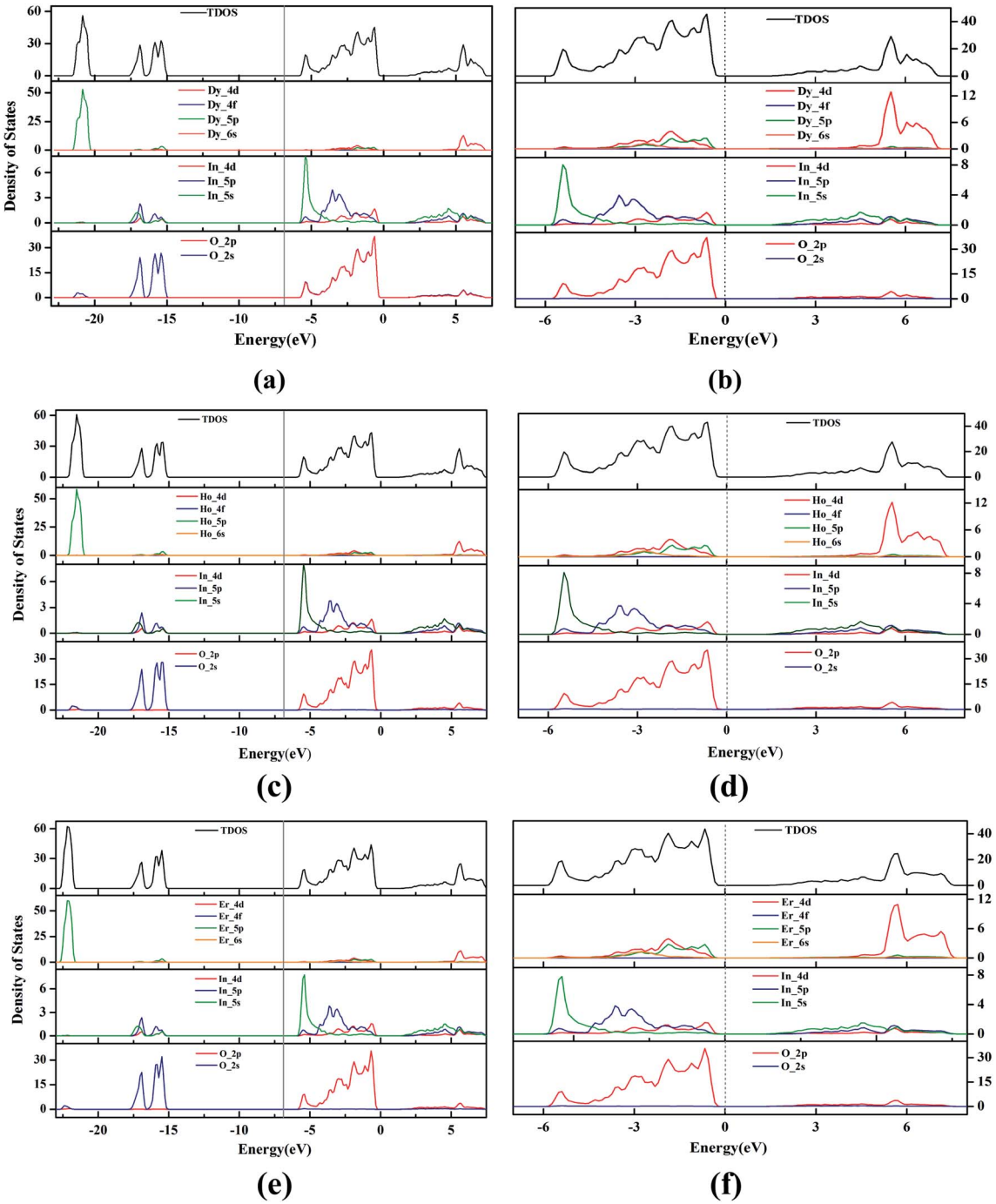

Fig. 3 The total and partial density of states of hexagonal $DyInO_3$ (a), $HoInO_3$ (c) and $ErInO_3$ (e) in the energy range from −27 to 7 eV and the enlarged map of $DyInO_3$ (b), $HoInO_3$ (d) and $ErInO_3$ (f) in energy range from −7 to 7 eV.

density of states near the valence band maximum (VBM) and the conduction band minimum (CBM), that is, in the energy range from −7 to 7 eV, as collected in Fig. 3(b), (d) and (f). From Fig. 3(b), we can see in the energy range from −7 to 0 eV the VBM of $DyInO_3$ mainly contributed by O 2p states, together with a part of contribution from In 4d states. Since the electronic contribution of Dy to partial density of states is less than 0.5 eV, therefore, we do not take the contribution of Dy into account. In the energy range from 0 to 7 eV, the CBM of $DyInO_3$ is mainly contributed by In 4d states, together with a small contribution from O 2p states. The density of In is much larger than the density of O in the contribution to the VBM, which indicates that a large part of the electrons of O transfer from the valence band to the conduction band and hybridize with Ti 3d electrons. For the case where the contribution of different atomic orbitals to the conduction band and the valence band of $RInO_3$, we can see similar situations in Fig. 3(d) and (f). The VBM and the CBM of these three structures are mainly contributed by O

and In, while the contribution of the lanthanides to the total density of states is not significant. This indicates that the band structure properties of hexagonal $DyInO_3$, $HoInO_3$ and $ErInO_3$ are mainly provided by the strong bonding of In and O whereas lanthanides show limited effects.

3.2 Dielectric properties of hexagonal $DyInO_3$, $HoInO_3$ and $ErInO_3$

We calculate the optical properties of hexagonal $DyInO_3$, $HoInO_3$ and $ErInO_3$ by calculating the static dielectric function $\varepsilon(\omega)$,

$$\varepsilon(\omega) = \varepsilon_1(\omega) + i\varepsilon_2(\omega) \quad (2)$$

where $\varepsilon_1(\omega)$ is the real part and $\varepsilon_2(\omega)$ is the imaginary part of the static dielectric function. The real part $\varepsilon_1(\omega)$ is characterized by the spontaneous polarization of the dielectric under an applied electric field, while the imaginary part $\varepsilon_2(\omega)$ is characterized by the loss of the dielectric and we can further calculate the optical properties of $RInO_3$ through imaginary parts.

Fig. 4(a) shows the real part curves of the static dielectric function of hexagonal $DyInO_3$, $HoInO_3$ and $ErInO_3$ and we can see that the static dielectric constants of these three crystals are all 4.53. The real part curves all reach the maximum when the photon energy reaches 2.24 eV. As shown in Fig. 4(b), the corresponding imaginary part curves of the dielectric function of $DyInO_3$, $HoInO_3$ and $ErInO_3$ show an increasing pattern in the energy range from 0 to 10.4 eV and decrease from 10.4 eV to 24.3 eV. All three systems under study give similar imaginary part curves, only with mutual shifts on peaks located in the energy range from 20 eV to 40 eV. It can be seen from Fig. 4(b) that the imaginary part function at 10.1 eV is much stronger than other dielectric function peaks, which corresponds to the transition of electrons from the O 2s valence band to the 4d conduction band of these three rare-earth elements. The peak at high energy (at around 28.0 eV) should be originated from the transition of electrons from the O 2p valence band to the 4d conduction band of rare-earth elements. The imaginary part function of $DyInO_3$ at 10.1 eV is slightly stronger than that of the other two materials. As the energy increases, the peaks show a blue-shift from $DyInO_3$ to $HoInO_3$ and to $ErInO_3$, which is consistent with the trend of the reflectivity curves of these three materials in Fig. 6(a) shown below.

3.3 Optical properties of hexagonal $DyInO_3$, $HoInO_3$ and $ErInO_3$

We calculated the real part $\varepsilon_1(\omega)$ and the imaginary part $\varepsilon_2(\omega)$ respectively of dielectric function of hexagonal $RInO_3$ in Perdew–Burke–Ernzerhof method by VASP and calculate the absorption spectrum coefficient $\alpha(\omega)$,[30,31]

$$\alpha(\omega) = \sqrt{2}\omega\left[\sqrt{\varepsilon_1^2(\omega) + \varepsilon_2^2(\omega)} - \varepsilon_1(\omega)\right]^{\frac{1}{2}} \quad (3)$$

Fig. 5(a) shows the absorption spectra of unit-cell hexagonal $DyInO_3$, $HoInO_3$ and $ErInO_3$ along the directions of *XX*, *YY* and *ZZ* respectively in the energy range from 0 to 60 eV. We can see from Fig. 5(a) that the absorption spectra of all three crystals are all very similar in the energy range from 0 to 25 eV. In the energy range from 25 to 30 eV, the absorption intensity of $ErInO_3$ at the absorption peak along the *XX* direction is significantly larger than that of $HoInO_3$, and the absorption intensity of $DyInO_3$ is the smallest among these three compounds, while their absorption intensity along the *ZZ* direction is equivalent. The absorption spectrum of $DyInO_3$ shows a distinct absorption peak at an energy of around 43 eV along all directions of *XX*, *YY* and *ZZ*, which is absent in the absorption spectra of both $ErInO_3$ and $HoInO_3$. The total absorption averaged over all three directions has been displayed in Fig. 5(b), from which we can see all three crystals show an absorption peak located at around 11 eV. Visible differences start to appear in the second peak region at around 30 eV. The three materials show very slight differences in peak intensities. A blue-shift of the peak can be observed with the decrease of atomic number of R. In addition, only $DyInO_3$ has a distinct absorption peak at the energy of around 43 eV.

We calculate the reflectivity $R(\omega)$ and refractive index $n(\omega)$ of all three crystals under study according to the imaginary part of the dielectric function,

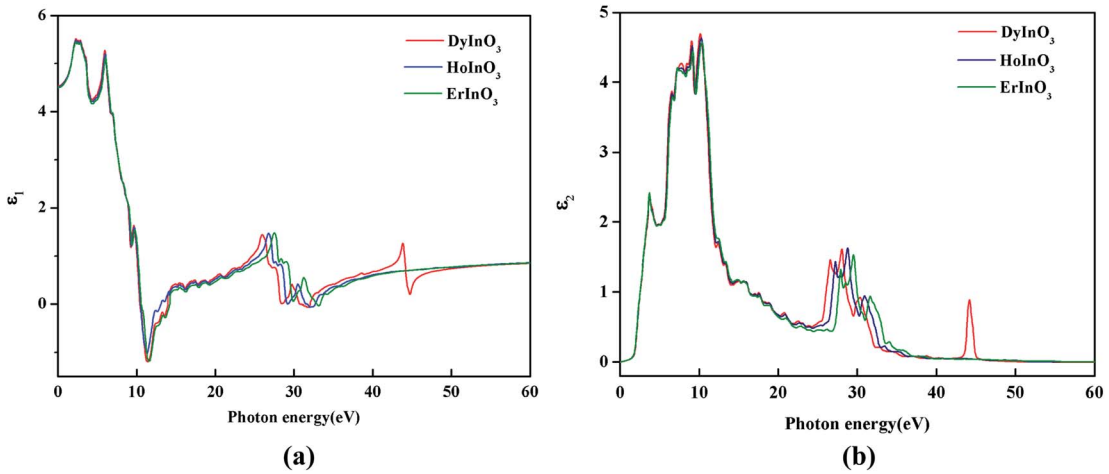

Fig. 4 The real part (a) and the imaginary part (b) of the static dielectric function of hexagonal $DyInO_3$, $HoInO_3$ and $ErInO_3$.

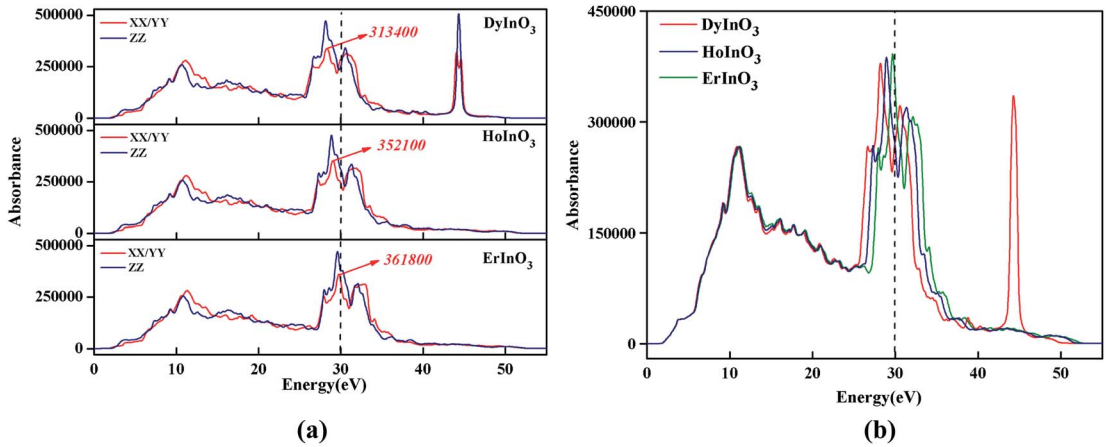

Fig. 5 Absorption spectra of hexagonal $DyInO_3$, $HoInO_3$ and $ErInO_3$ along different directions respectively (a) and their comparison of total absorption spectra (b) in energy range from 0 to 60 eV.

$$R(\omega) = \left| \frac{\sqrt{\varepsilon_1(\omega) + i\varepsilon_2(\omega)} - 1}{\sqrt{\varepsilon_1(\omega) + i\varepsilon_2(\omega)} + 1} \right|^2 \quad (4)$$

$$n(\omega) = \frac{1}{\sqrt{2}} \left\{ \left[\varepsilon_1{}^2(\omega) + \varepsilon_2{}^2(\omega) \right]^{\frac{1}{2}} + \varepsilon_1(\omega) \right\}^{\frac{1}{2}} \quad (5)$$

Fig. 6(a) shows the reflectivity of hexagonal $DyInO_3$, $HoInO_3$ and $ErInO_3$, from which we can see that the strongest peak locates at around 10 eV. A similar trend as the absorption spectra can be found for the second peak which shows a shift with the increase of atomic number of R. Again, only $DyInO_3$ has a reflectance peak at the energy of around 45 eV, the same as observed in the absorption spectra. In the energy range from 0 to 6 eV and 12 to 32 eV, the reflectivity curve of hexagonal $RInO_3$ is lower than 0.2, showing that these three structures are transparent for photons in these energy ranges.

Fig. 6(b) shows the refractive index of unit-cell hexagonal $DyInO_3$, $HoInO_3$ and $ErInO_3$. The refractive peak in the energy range from 0 to 10 eV arise from the transition from the O 2p to In 5s states, while a relatively small refractive peak at an energy of around 26 eV corresponds to the transition from the In 5p states to the conduction band. We can see from the figure that the static refractive index of $DyInO_3$, $HoInO_3$ and $ErInO_3$ are calculated to be 2.130, 2.127 and 2.124 respectively, which are in good consistency with the trend in the dielectric constant curve as shown in Fig. 4(a). The high refractive index of $DyInO_3$, $HoInO_3$ and $ErInO_3$ appearing in the low energy range reflect a high band gap,[32,33] which is consistent with the band structure calculations.

We calculate the electron energy loss function $L(\omega)$ and molar extinction coefficient $k(\omega)$ of hexagonal $DyInO_3$, $HoInO_3$ and $ErInO_3$ according to the imaginary part of the dielectric function,

$$L(\omega) = \frac{\varepsilon_2(\omega)}{\varepsilon_1{}^2(\omega) + i\varepsilon_2{}^2(\omega)} \quad (6)$$

$$k(\omega) = \frac{1}{\sqrt{2}} \left\{ \left[\varepsilon_1{}^2(\omega) + \varepsilon_2{}^2(\omega) \right]^{\frac{1}{2}} - \varepsilon_1(\omega) \right\}^{\frac{1}{2}} \quad (7)$$

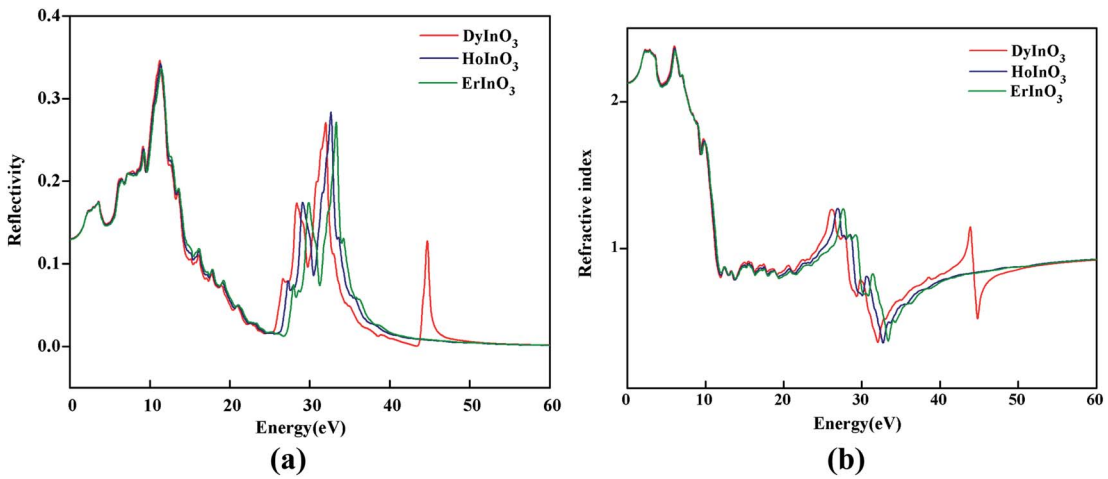

Fig. 6 The reflectivity (a) and refractive index (b) of hexagonal $DyInO_3$, $HoInO_3$ and $ErInO_3$.

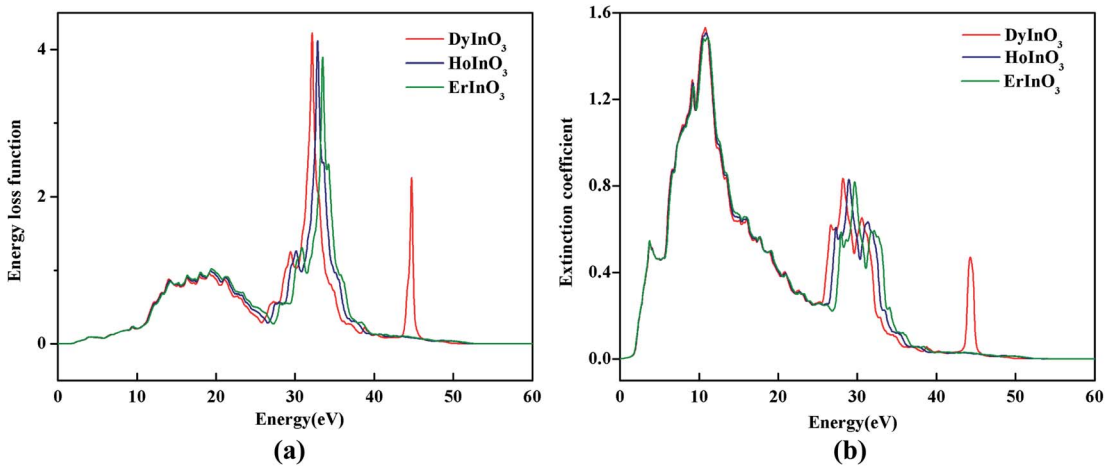

Fig. 7 The electron energy loss spectrum (a) and molar extinction coefficient (b) of hexagonal $DyInO_3$, $HoInO_3$ and $ErInO_3$.

Fig. 7(a) shows the electron energy loss spectrum of hexagonal $DyInO_3$, $HoInO_3$ and $ErInO_3$. The electron energy loss spectrum is the inelastic scattering of the incident electron beam in $DyInO_3$, $HoInO_3$ and $ErInO_3$, and explores the electronic structure of them. We can see from Fig. 7(a) that there are 5 weak peaks in the electron energy loss spectrum of $DyInO_3$, $HoInO_3$ and $ErInO_3$ in the energy range from 14 to 21 eV. At an energy of around 33 eV, they both have a narrow and sharp peak and the ordering of the energy loss function is $DyInO_3$ > $HoInO_3$ > $ErInO_3$. The peaks of $DyInO_3$, $HoInO_3$ and $ErInO_3$ occur at the energy of 32.2 eV, 33.0 eV and 33.5 eV respectively, which are related to the decrease of refractive index of $DyInO_3$, $HoInO_3$ and $ErInO_3$ as shown in Fig. 6(b). It indicates that the unit-cell of hexagonal $DyInO_3$, $HoInO_3$ and $ErInO_3$ can be used as effective optical storage materials at the energy of around 33 eV.

Molar extinction coefficient, also known as molar absorptivity, refers to the extinction coefficient at a concentration of 1 mol L^{-1}. When the unit of concentration is expressed in g L^{-1}, the molar absorptivity $k(\omega)$ is numerically equal to the product of the extinction coefficient and the molecular weight (M) of the substance,

$$k(\omega) = \alpha(\omega)M \quad (8)$$

Fig. 7(b) shows the molar extinction coefficient of unit-cell hexagonal $DyInO_3$, $HoInO_3$ and $ErInO_3$. We can see the extinction peaks of $DyInO_3$, $HoInO_3$ and $ErInO_3$ are the same as their absorption peaks at the energy of around 30 eV. However, unlike the trend of the absorption spectrum, the extinction peaks appearing at around 12 eV are larger than the extinction peak at 30 eV, which is also in good consistency with the trend of the reflectivity curves as shown in Fig. 6(a).

4 Conclusions

In this paper, we have studied the electronic structure, the optical and dielectric properties of hexagonal $DyInO_3$, $HoInO_3$ and $DyInO_3$ by performing first principles studies. After optimization, the lattice parameters are in great agreement with the experimental values within an error of 1%. Our calculation has determined that the three hexagonal $RInO_3$ in present study are indirect band gap crystals with band-gap values decreasing with the increase of atomic number. DOS calculations indicate that the electronic properties of hexagonal $DyInO_3$, $HoInO_3$ and $ErInO_3$ are mainly provided by the strong bonding of In and O whereas lanthanides show limited effect. The dielectric properties and ionic contribution are calculated and a comparison has been made on the dielectric function including the static dielectric tensor. We have also calculated the absorption coefficient, the reflectivity, the refractive index, the conductivity and the electron energy-loss spectrum of hexagonal $DyInO_3$, $HoInO_3$ and $DyInO_3$. The present study reveals that the dependence of the optical and dielectric properties of $RInO_3$ on the rare-earth atomic number is not evident, which also can be a useful guideline in the manufacture of multifunctional devices based on $RInO_3$.

Conflicts of interest

There are no conflicts to declare.

Acknowledgements

We acknowledge the National Nature Science Foundation of China (Grant No. 21573129 and 21403300). The authors also acknowledge a generous grant of computer time from the National Supercomputer Center in Tianjin-TianHe-1(A).

References

1 D. W. Bondurant and F. P. Gnadinger, Ferroelectrics for nonvolatile RAMs, *IEEE Spectrum*, 1989, **26**, 30–33.
2 C. A. -Paz de Araujo, J. D. Cuchiaro, L. D. McMillan, M. C. Scott and J. F. Scott, Fatigue-free ferroelectric capacitors with platinum electrodes, *Nature*, 1995, **374**, 627–629.

3 R. Ramesh and N. A. Spaldin, Multiferroics: progress and prospects in thin films, *Nat. Mater.*, 2007, **6**, 21–29.
4 M. Bibes and A. Barthélémy, Towards a magnetoelectric memory, *Nat. Mater.*, 2008, **7**, 425–426.
5 E. Cockayne and B. P. Burton, Phonons and Static Dielectric Constant in $CaTiO_3$ from First Principle, *Phys. Rev. B: Condens. Matter Mater. Phys.*, 2000, **62**, 3735.
6 G. A. Samara, The relaxational properties of compositionally disordered ABO_3 perovskites, *J. Phys.: Condens. Matter*, 2003, **15**, R367–R411.
7 T. Katsufuji, M. Masaki, A. Machida, M. Moritomo, K. Kato, E. Nishibori, M. Takata, M. Sakata, K. Ohoyama, K. Kitazawa and H. Takagi, Crystal structure and magnetic properties of hexagonal $RMnO_3$ (R=Y, Lu and Sc) and the effect of doping, *Phys. Rev. B: Condens. Matter Mater. Phys.*, 2002, **66**, 134434.
8 C. J. Fennie and K. M. Rabe, Polar phonons and intrinsic dielectric response of the ferromagnetic insulating spinel $CdCr_2S_4$ from first principles, *Phys. Rev. B: Condens. Matter Mater. Phys.*, 2005, **72**, 1–4.
9 Q. Zhang, G. Tan, L. Gu, Y. Yao, C. Jin, Y. Wang, X. Duan and R. Yu, Direct Observation of Multiferroic Vortex Domains in $YMnO_3$, *Sci. Rep.*, 2013, **3**, 1–5.
10 M. G. Han, Y. Zhu, L. Wu, T. Aoki, V. Volkow, X. Wang, S. C. Chae, Y. S. Oh and S. W. Cheong, Ferroelectric Switching Dynamics of Topological Vortex Domains in a Hexagonal Manganite, *Adv. Mater.*, 2013, **25**, 2415–2421.
11 M. Lilienblum, T. Lottermoser, S. Manz, S. M. Selbatch, A. Cano and M. Fiebig, Ferroelectricity in the multiferroic hexagonal manganites, *Nat. Phys.*, 2015, **11**, 1070–1073.
12 B. B. V. Aken, T. T. M. Palstra, A. Filippetti and N. A. Spaldin, The origin of ferroelectricity in magnetoelectric $YMnO_3$, *Nat. Mater.*, 2004, **3**, 164–170.
13 Z. J. Huang, Y. Cao, Y. Y. Xue and C. W. Chu, Coupling between the ferroelectric and antiferromagnetic orders in $YMnO_3$, *Phys. Rev. B: Condens. Matter Mater. Phys.*, 1997, **56**, 2623.
14 C. L. Lin, J. Liu, Y. C. Lin, X. D. Li and R. Li, Pressure-induced structural and vibrational evolution in ferroelectric $RInO_3$ (R=Eu, Gd, Dy), *Solid State Commun.*, 2013, **173**, 51–55.
15 Y. B. Li, Y. Z. Wang, W. J. Tan, W. B. Wang, J. J. Zhang, J. W. Kim, S. W. Cheong and X. T. Tao, Laser floating zone growth of improper geometric ferroelectric $GdInO_3$ single crystals with Z_6 topological defects, *J. Mater. Chem. C*, 2018, **6**, 7024.
16 S. C. Abrahams, Ferroelectricity and structure in the $YMnO_3$ family, *Acta Crystallogr., Sect. B: Struct. Sci.*, 2001, **57**, 485–490.
17 R. Shukla, V. Grover, S. K. Deshpande, D. Jain and A. K. Tyagi, Synthesis and Structural and Electrical Investigations of a Hexagonal Y1–xGdxInO$_3$ ($0.0 \leq x \leq 1.0$) System Obtained via Metastable C-Type Intermediates, *Inorg. Chem.*, 2013, **52**, 13179–13187.
18 R. Shukla, F. N. Sayed, V. Grover, S. K. Deshpande, A. Guleria and A. K. Tyagi, Quest for Lead Free Relaxors in YIn1–*x*Fe*x*O$_3$ ($0.0 \leq x \leq 1.0$) System: Role of Synthesis and Structure, *Inorg. Chem.*, 2014, **53**, 10101–10111.
19 V. Grover, R. Shukla, D. Jain, S. K. Deshpande, A. Arya, C. G. S. Pillai and A. K. Tyagi, Complex GdSc1–*x*In*x*O$_3$ Oxides: Synthesis and Structure Driven Tunable Electrical Properties, *Chem. Mater.*, 2012, **24**, 2186–2196.
20 B. Paul, S. Chatterjee, S. Gop, A. Roy, V. Grover, R. Shukla and A. K. Tyagi, Evolution of lattice dynamics in ferroelectric hexagonal $REInO_3$ (RE = Ho, Dy, Tb, Gd, Eu, Sm) perovskites, *Mater. Res. Express*, 2016, **3**, 075703.
21 H. Sawamoto, High-Pressure Synthesis of Perovskite Type $RInO_3$(R=Eu, Gd, and Dy), *Jpn. J. Appl. Phys.*, 1973, **12**, 1432.
22 T. Tohei, H. Moriwake, H. Murata, A. Kuwabara, R. Hashimoto, T. Uamamoto and I. Tanaka, Geometric ferroelectricity in rare-earth compounds $RGaO_3$ and $RInO_3$, *Phys. Rev. B: Condens. Matter Mater. Phys.*, 2009, **79**, 744125.
23 C. W. F. T. Pistorius and G. J. Kruger, Stability and structure of noncentrosymmetric hexagonal $LnInO_3$ (Ln = Eu, Gd, Tb, Dy, Ho, Y), *J. Inorg. Nucl. Chem.*, 1976, **38**, 1471.
24 J. P. Perdew, K. Burke and M. Ernzerhof, Generalized Gradient Approximation Made Simple, *Phys. Rev. Lett.*, 1996, **77**, 3865.
25 G. Kresse and J. Furthmüller, Efficient iterative schemes for ab initio total-energy calculations using a plane-wave basis set, *Phys. Rev. B: Condens. Matter Mater. Phys.*, 1996, **54**, 11169.
26 G. Kresse and J. Furthmüller, Efficiency of ab-initio total energy calculations for metals and semiconductors using a plane-wave basis set, *Comput. Mater. Sci.*, 1996, **6**, 15.
27 H. J. Monkhorst and J. D. Pack, Special points for Brillouin-zone integrations, *Phys. Rev. B: Solid State*, 1976, **13**, 5188–5192.
28 C. W. F. T. Pistorius and G. J. Kruger, Stability and structure of noncentrosymmetric hexagonal $LnInO_3$ (Ln = Eu, Gd, Tb, Ho, Y), *J. Inorg. Nucl. Chem.*, 1976, **38**, 1471–1475.
29 S. J. Clark, M. D. Segall, C. J. Pickard, P. J. Hasnip, M. I. J. Probert, K. Refson and M. C. Payne, First principles methods using CASTEP, *Z. Kristallogr.*, 2005, **220**, 567–570.
30 S. Saha, T. P. Sinha and A. Mookerjee, Electronic structure, chemical bonding, and optical properties of paraelectric $BaTiO_3$, *Phys. Rev. B: Condens. Matter Mater. Phys.*, 2000, **62**, 8828–8834.
31 C. Chen, T. Sasaki, R. Li, Y. Wu, Z. Lin, Y. Mori, Z. Hu, J. Wang, G. Aka, M. Yoshimura and others, Theoretical Basis for the Development of Borate Nonlinear Optical Crystals, *Nonlinear Optical Borate Crystals, Principals and Applications*, John Wiley & Sons, 2012.
32 B. Luo, X. Wang, E. Tian, G. Li and L. Li, Electronic structure, optical and dielectric properties of $BaTiO_3$/$CaTiO_3$/$SrTiO_3$ ferroelectric superlattices from first-principles calculations, *J. Mater. Chem. C*, 2015, **3**, 8625–8633.
33 X. D. Zhang, M. L. Guo, W. X. Li and C. L. Liu, First-principle study of electronic and optical properties in wurtzite Zn1-xCdxO, *J. Appl. Phys.*, 2008, **103**, 063721.

